Application of a Bayesian Wind Profile Retrieval Technique to Radar Data Collected in the Alpine Southern Upslope Region and Comparison with Upstream Wind Profiler Measurements

Pierre Tabary, Monique Petitdidier

Application of a Bayesian Wind Profile Retrieval Technique to Radar Data Collected in the Alpine Southern Upslope Region and Comparison with Upstream Wind Profiler Measurements

P. TABARY AND M. PETITDIDIER

Centre d'Étude des Environnements Terrestre et Planétaires, Velizy, France

(Manuscript received 25 June 2001, in final form 16 October 2001)

ABSTRACT

In this paper, a new operational technique to retrieve the horizontal wind profile from Doppler radar measurements is used to carry out a statistical comparison of upslope and upstream wind profiles in the southern flank of the European Alps. The method relies upon a first-order velocity azimuth display (VAD) expansion of the radial velocity and allows for recovering, through Bayesian updates, the likeliest wind speed and direction at each height. The major advantage of this new approach over existing ones is that it does not require any preliminary dealiasing of the radar data. This original feature makes it very well suited to real-time operational purposes. The method has been applied to 1248 volumetric sequences collected during the recent Mesoscale Alpine Programme (MAP) experiment by the Swiss C-band Monte Lema radar located in the alpine upslope region. The resulting profiles are compared to simultaneous measurements obtained upstream by the French Institut National des Sciences de l'Univers (INSU)/Météo-France VHF wind profiler. This extensive comparison allows validating of the proposed Bayesian VAD and inferring of some statistical properties of the wind profile during precipitation events in the southern Alps.

1. Introduction

Weather Doppler radars (hereafter referred to as WDRs) and wind profilers (hereafter referred to as WPs) are among the most widespread instruments in observational operational networks. A common feature of these two instruments is their ability to be integrated in networks [see e.g., Serafin and Wilson (2000) for a description of the U.S. Next Generation Weather Radar (NEXRAD) network and Caccia et al. (2001) for a recent implementation of a wind profiler network]. Year after year, WDRs have become key instruments in the fields of cloud studies, hydrology, and nowcasting because they provide a three-dimensional convective-scale view of precipitating systems with a high temporal resolution (5 min) over mesoscale and even synoptic-scale domains. Kinematic parameters, such as vertical profiles of wind speed and direction, can also be extracted from the radar dataset by application of algorithms such as the velocity azimuth display (VAD; see Browning and Wexler 1968) or velocity volume processing (VVP; see Waldteufel and Corbin 1979). One of the main drawbacks of radars, however, is that they cannot measure (at least outside the boundary layer) the environment above and around precipitating systems, which often prove to be key elements in understanding their kinematic and microphysical evolution. WPs, on the other hand, do not suffer from that limitation and provide vertical wind profiles on a regular basis with a high spatial (~300 m) and temporal (~15 min) resolution. This is undoubtedly one of the reasons why WP data, unlike WDR data, have very early been assimilated in numerical weather prediction models [see the recent review of Rossa (2000) on the current state-of-the-art WDR data assimilation]. However, their measurements are basically one-dimensional and can be very difficult to interpret without any additional information on the spatial distribution of the observed system around the WP.

During the recent field phase of the Mesoscale Alpine Programme (MAP; see Bougeault et al. 2001), a number of instruments were deployed in the southern flank of the Alps, in the so-called Lago Maggiore Target Area (LMTA), in order to document atmospheric and hydrological processes over complex terrain. In particular, the experimental setup comprised research weather Doppler radars such as the French C-band Ronsard radar (CETP) and the American National Center for Atmospheric Research (NCAR) S-band dual-polarization Doppler (S-Pol) radar in order to ensure, along with existing radars such as the operational Swiss C-band Monte Lema radar (SMA), a coverage of alpine precipitating systems with a unique spatial and temporal resolution. Two wind pro-

Corresponding author address: Pierre Tabary, DSO/CMR, Météo-France, 7 Rue Teissererc-de-Bort, 78195 Trappes, France.
E-mail: tabary@cetp.ipsl.fr

filers, UHF and VHF [Institut National des Sciences de l'Univers (INSU)/Météo-France], were also nested in the multiple-Doppler network in order to collect information on the boundary layer and upper-level flow structures. Over the two months and one week of the special observing period (SOP; 7 September 1999–15 November 1999), a huge amount of data were collected simultaneously by WP and WDR. The present paper is part of a series devoted to the exploration of the various possible synergies between those complementary instruments. The MAP dataset is used to evaluate the potential of each approach.

In a recent paper, Petitdidier et al. (2000), following Guillemette and Zawadzki (1999), investigated the impact of the integration of the WP data in a dual-Doppler wind synthesis. Using simulated and real data, they found that the main impact is very local and that the retrieved wind components are only slightly modified just above the WP. This can heuristically be explained by the fact that the volume of information provided by the WP is very small in comparison with the three-dimensional dataset of the dual-Doppler system. In one very specific geometrical configuration, however, when the WP is located along the dual-Doppler radar baseline, Petitdidier et al. (2000) found that the impact of the integration of the WP data becomes significant and helps better conditioning the wind retrieval in a region where the radar beams are nearly colinear. Finally, in some cases, the WP was useful in precisely defining the appropriate lower- and upper-boundary conditions that are required to integrate vertically the mass continuity equation and correctly retrieve the vertical velocity from the column of horizontal divergence.

In the present paper, we take advantage of the MAP experimental setup in a different way and compare a set of more than 1200 WDR wind profiles, retrieved by means of a new VAD-based Bayesian method, with simultaneous WP measurements. The WP and WDR considered for this comparison are, respectively, the French VHF wind profiler, located south of the Alps in the plains of northern Italy, and the Monte Lema WDR, located 50 km to the north of the WP in the alpine upslope region. Unlike most of the previous VAD-based analysis, the present method, initially proposed by Tabary et al. (2000), does not require any preliminary dealiasing of the radial velocities. This original feature makes it very well suited to operational use in a real-time context. The experimental setup and the sampling strategies of both instruments during MAP are described in section 2. Section 3 gives the basic formulation and the possible optimizations and refinements of the Bayesian VAD. Given the geographical positions of the two instruments considered in the present paper, this work also permits assessment of some robust statistical features of upslope precipitation events in the southern Alps. Results are summarized in section 4.

2. Experimental setup

Figure 1 is a topographical map of the Alpine ridge centered on the Lago Maggiore region, which corresponds, according to the high-resolution precipitation climatalogy of the Alps by Frei and Schär (1998), to the climatological maximum of the Alps for heavy precipitation events during the fall. This statistical feature can be linked to its location, in the alpine southern upslope region, right at the intersection of the alpine arc-shaped ridge with the low, flat plains of northern Italy. These plains act as natural channels for the warm moist air masses originating from the Adriatic Sea to the east and from the Ligurian Sea to the south.

The INSU/Météo-France VHF WP, denoted by ST, and the operational Swiss C-band Monte Lema WDR (SMA) are also indicated in Fig. 1. Their geographical positions and technical characteristics are summarized in Table 1. All heights hereafter, unless otherwise stated, are relative to the mean sea level (MSL). As can be seen in Fig. 1, the WP was located in the plains (Lonate Pozolo, Italy) at about 53 km to the south of the operational Monte Lema WDR located in the Alpine upslope region.

During the MAP field phase (7 September–15 November 1999), the repetition time of the VHF WP was 15 min and its vertical resolution 300 m. Each profile starts at the height of 1.5 km and ends at a height of 16 km. On the other hand, the sampling mode of the operational Monte Lema WDR consists of a complete volumetric exploration every 5 min. Each volume comprises 20 sweeps of increasing elevation: $-0.3°$, $0.5°$, $1.5°$, $2.5°$, $3.5°$, $4.5°$, $5.5°$, $6.5°$, $7.5°$, $8.5°$, $9.5°$, $11.0°$, $13.0°$, $15.5°$, $18.3°$, $21.6°$, $25.3°$, $29.6°$, $34.5°$, and $40.5°$. The gate width along each ray is 1000 m, and the maximum range for the Doppler velocity is 130 km. The Nyquist velocity of the radar ranges from 8.27 m s^{-1} for the lowest elevation angles up to 16.54 m s^{-1} for the highest ones [see Joss et al. (1998) for further details].

3. A real-time algorithm to retrieve the wind profile from raw WDR data

a. Motivations

In order to allow comparison between WDR and WP measurements, the three-dimensional WDR dataset is reduced to a vertical profile of wind speed and direction. This can be done by applying the classical VAD analysis. The VAD analysis, formerly proposed by Lhermitte and Atlas (1961) and extended by Browning and Wexler (1968), relies entirely upon the assumption of linearity of the wind field. Under that assumption, it can be shown that the radial velocity, which is the projection of the hydrometeor velocity along the radar beam, identifies with a second-order Fourier series of the radar azimuth. For the present application, we truncate the

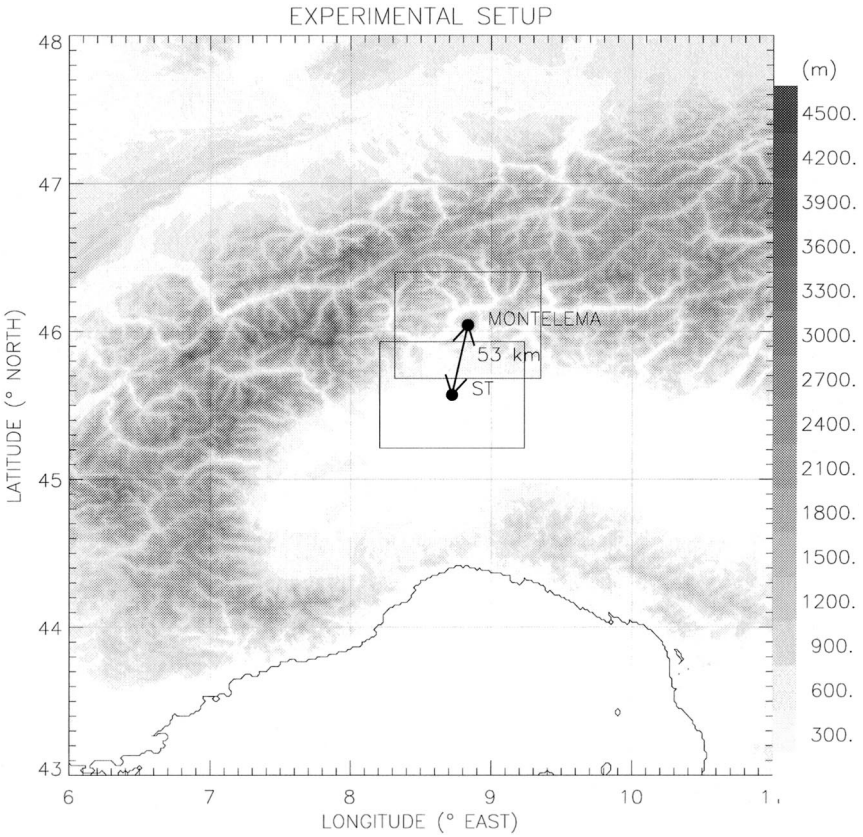

FIG. 1. Topographical map of the alpine ridge showing the positions of the Swiss C-band Monte Lema radar and the French VHF wind profiler (denoted by ST). Note the numerous deep valleys that penetrate the large-scale arc-shaped range, especially the one (called the Ticino valley) to the west of the Monte Lema WDR. The two 80 km × 80 km boxes centered on the WDR and on the WP are the domains over which the Contoured Frequency per Altitude Diagrams were computed (see Fig. 3).

expansion to the first-order terms. Thus, the radial velocity V_r reads

$$V_r = a_0 + a_1 \cos\theta + b_1 \sin\theta. \quad (1)$$

with the corresponding expressions for the Fourier coefficients,

$$a_0 = (w_0 - v_T) \sin\varphi + \frac{r \cos^2\varphi}{2}\underbrace{\left[\left(\frac{\partial u}{\partial x}\right)_0 + \left(\frac{\partial v}{\partial y}\right)_0\right]}_{\mathrm{DIV}_0}, \quad (2)$$

$$a_1 = v_0 \cos\varphi, \quad (3)$$

$$b_1 = u_0 \cos\varphi, \quad (4)$$

where θ stands for the azimuth; φ for the elevation angle; r for the range; v_T for the terminal fall speed of hydrometeors; and u_0, v_0, w_0, and DIV_0 for the wind components and divergence at the radar location (O), respectively. From Eq. (1), the Fourier coefficients, that is, a_0, a_1, and b_1, can be very easily determined from the data allowing, in a second step, the horizontal wind components to be retrieved. However, one major requirement of the application of the VAD analysis is that radial velocities first have to be corrected for aliasing.

Aliasing occurs when the real radial velocity exceeds the Nyquist thresholds ($\pm V_r^N$) of the radar, which are determined by the radar wavelength and its pulse repetition frequency (PRF) according to (Doviak and Zrnić 1984)

$$V_r^N = \frac{\lambda f_r}{4}, \quad (5)$$

where λ is the radar wavelength. Radial velocities with amplitude greater than the Nyquist velocity will appear aliased, that is, shifted by $\pm 2kV_r^N$, where k is an integer, into the Nyquist interval $[-V_r^N \cdot V_r^N]$.

Considering that the Nyquist velocities of the Monte Lema WDR are rather low (from 8.27 up to 16.54 m s^{-1}), aliasing occurs frequently, so that the Monte Lema data are particularly well suited to testing the Bayesian method of Tabary et al. (2000), which is designed to retrieve the wind profile under aliasing conditions.

b. Basic formulation

For simplicity, all of the following developments are achieved at a given vertical level z_0.

1) A VAD-BASED MODEL FOR THE RADIAL VELOCITY

We first rewrite Eq. (1) as a function of the wind speed (U_0) and direction (θ_0), with the specific (nonmeteorological) convention $\theta_0 = +90°$ for a westerly wind:

$$V_r = a_0 + U_0 \cos\varphi \cos(\theta - \theta_0). \tag{6}$$

The a_0 coefficient of Eq. (6) then has to be explicitly specified. The contribution of the terminal fall speed can be determined from the reflectivity value on the basis of empirical relationship (Battan 1977), whereas in a first step the contribution of the horizontal divergence and of the vertical velocity can be neglected. This is a further hypothesis of the application of the Bayesian scheme; however, according to Eq. (2), at low elevation angles and short ranges from the radar, the contribution of these two terms (horizontal divergence and vertical velocity) in the radial velocity can be neglected with a high degree of confidence.

2) DEFINITION OF THE POSSIBLE VALUES FOR THE WIND SPEED AND DIRECTION AND INTRODUCTION OF THE PROBABILITY ARRAY

The next step is the definition of the possible values for the wind speeds U_0 and directions θ_0. A priori, θ_0 may vary from 0° to 360°, and U_0 from 0 to 50 m s^{-1} (if one considers that the maximum observable wind speed is less than 50 m s^{-1}). The number of elements of the collection then has to be chosen. A large number of possible values will allow a fine description but will require more computing time, so that a trade-off has to be found. In the next section, refinements and optimizations are presented to meet simultaneously these two requirements. From now on, possible wind speeds are indexed by $i(U_0^i)$ and possible wind directions by $j(\theta_0^j)$, whereas the *real* wind speed and direction to be estimated will be denoted by U_0 and θ_0. A probability $p(i, j)$ is then assigned to each couple (U_0^i, θ_0^j). The basic idea of the method is to update this array of probabilities by considering, in turn, each measurement of the radar sequence and to deduce from the initial array of possible speeds and directions the most likely ones. Initially, if no information is available, all probabilities are equal, which means that all couples (U_0^i, θ_0^j) are a priori equally possible.

3) UPDATING FORMULA FOR THE PROBABILITY ARRAY

Under the assumption that N measurements have already been taken into account and that a new measurement (characterized by the azimuth θ^{N+1}, the elevation φ^{N+1}, and the radial velocity V_r^{N+1}) is collected, the updating formula for the probabilities $[p^N(i, j) \Rightarrow p^{N+1}(i, j)]$ is given by the Bayesian rule on conditional probabilities (Mood et al. 1963):

$$P(A|B) = \frac{P(A) \times P(B|A)}{P(B)}, \tag{7}$$

where A and B are two events and $P(A|B)$ stands for the conditional probability of A if B. Applied to our problem, it can be rewritten as

$$\begin{aligned} &P[(U_0, \theta_0) = (U_0^i, \theta_0^j)|(\theta, \varphi, V_r) = (\theta^{N+1}, \varphi^{N+1}, V_r^{N+1})] \\ &= \frac{P[(U_0, \theta_0) = (U_0^i, \theta_0^j)] \times P[(\theta, \varphi, V_r) = (\theta^{N+1}, \varphi^{N+1}, V_r^{N+1})|(U_0, \theta_0) = (U_0^i, \theta_0^j)]}{P[(\theta, \varphi, V_r) = (\theta^{N+1}, \varphi^{N+1}, V_r^{N+1})]}. \end{aligned} \tag{8}$$

Each term of Eq. (8) can be expressed as follows:

$$\begin{aligned} &P[(U_0, \theta_0) = (U_0^i, \theta_0^j)|(\theta, \varphi, V_r) = (\theta^{N+1}, \varphi^{N+1}, V_r^{N+1})] \\ &\quad = p^{N+1}(i, j), \end{aligned} \tag{9}$$

$$P[(U_0, \theta_0) = (U_0^i, \theta_0^j)] = p^N(i, j), \tag{10}$$

$$\begin{aligned} &P[(\theta, \varphi, V_r) = (\theta^{N+1}, \varphi^{N+1}, V_r^{N+1})] \\ &\quad = \sum_{i,j} p^N(i, j) \\ &\qquad \times P[(\theta, \varphi, V_r) = (\theta^{N+1}, \varphi^{N+1}, V_r^{N+1})|(U_0, \theta_0) \\ &\qquad\quad = (U_0^i, \theta_0^j)]. \end{aligned} \tag{11}$$

Thus, it can be seen from Eqs. (9)–(11) that only one probability has to be specified ($P[(\theta, \varphi, V_r) = (\theta^{N+1}, \varphi^{N+1}, V_r^{N+1})|(U_0, \theta_0) = (U_0^i, \theta_0^j)]$). It is the probability to observe, for the azimuth θ and the elevation φ, the value V_r for the radial velocity under the assumption that the real wind speed and direction (U_0 and θ_0) are, respectively, U_0^i and θ_0^j. We denote that probability by $\pi^{i,j}(V_r)$. Equation (8) then simply reads

$$p^{N+1}(i, j) = p^N(i, j) \times \frac{\pi^{i,j}(V_r)}{\sum_{i,j} p^N(i, j) \times \pi^{i,j}(V_r)}. \tag{12}$$

TABLE 1. Geographical positions and technical characteristics of the WP and WDR used in the present study.

	Monte Lema WDR/ SMA Switzerland	VHF INSU/Météo-France France
Lat	46.042°N	45.47°N
Lon	8.833°E	8.72°E
Alt	1625 m	146 m
Frequency	5.6 GHz	45 MHz

4) AN ANALYTICAL EXPRESSION FOR $\pi^{i,j}(V_r)$

Given our linear model [Eq. (6)], the azimuth (θ) and elevation (φ) angles, the (i, j)th predicted value of the radial velocity reads

$$V_r^{i,j} = a_0 + U_0^i \cos\varphi \cos(\theta - \theta_0^j). \tag{13}$$

The dispersion of the measured radial velocities around that model sine profile results either from instrumental noise or from model errors (i.e., nonlinearities of the actual wind field and unperfectness of the parameterization of the a_0 term), or even from velocity aliasing. To account for these three sources of dispersion, the following expression for $\pi^{i,j}(V_r)$ is proposed:

$$\pi^{i,j}(V_r) = \frac{\left\{1 + \cos\left[\frac{\pi}{V_r^N}(V_r - V_r^{i,j})\right]\right\}^n}{N(n)}, \tag{14}$$

where $N(n)$, n being an integer, is a normalization factor equal to $[2\,V_i^N(2n)!]/[2^n(n!)^2]$. The special dependence of $\pi^{i,j}(V_r)$, through a cosine function, on the difference between the observed and predicted radial velocities ($V_r - V_r^{i,j}$) allows overcoming of the problem of possible aliasing of the observed radial velocities. Indeed, this amounts to calculating the distance between the two radial velocities (measured and predicted) modulo the Nyquist interval. The parameter n controls the decreasing rate of the probability around its maximum value. High (low) values of n determine sharply peaked (smoothly peaked) distributions of the probability around the maximum. A value of 1 for n proved to be physically consistent with the typical dispersion around the sine profile.

5) FINAL ESTIMATION OF THE WIND SPEED AND DIRECTION

Finally, once all measurements of the radar sequence have been taken into account, the estimated wind direction and speed can be either chosen as the ones among the possible speeds and directions with the highest final probability or computed as the sum over all possible states weighted by the final probabilities $[p^\infty(i, j)]$. Thus,

$$\hat{U}_0 = \sum_i \left[\sum_j p^\infty(i, j)\right] U_0^i \tag{15}$$

$$\hat{\theta}_0 = \sum_j \left[\sum_i p^\infty(i, j)\right] \theta_0^j. \tag{16}$$

Practically, we have observed that there is almost no difference between those two estimators, so for the sake of simplicity we retained the first one. Figure 2 is an illustration of the application of the method on a particular case (1250 UTC 20 September 1999) showing the observed radial velocities (white dots) as functions of the azimuth as well as the retrieved wind speed and direction (sine curve). The occurrence probability of the radial velocities associated to the retrieved wind speed and direction ($U_0^i = 47$ m s^{-1} and $\theta_0^j = 0$) is given by Eq. (14) and has been superimposed on Fig. 2.

c. Refinements and optimizations

As explained in the previous section, a trade-off has to be found between the computing time and the resolution of the analysis in terms of wind speed and direction. A speed step of 2 m s^{-1} and a direction step of 5° require, with the [0, 50] m s^{-1} and [0, 360] degrees bounds, 1846 elements in the collection. It means that, for *each* radial velocity measurement, 1846 evaluations of the predicted radial velocity and 1846 updates have to be performed. Considering that operational Doppler radars typically gather 10^4–10^5 observations in a volumic sequence, the operational implementation of the method in its basic formulation might appear impossible. This is why we propose, in this section, some ways to speed up the method while keeping a good resolution for the wind speed and direction.

The first one consists of using a first guess of the wind speed (U_0^b) and direction (θ_0^b), resulting either from a previous analysis or from model output, or even from a radiosounding. The range of possible values for the wind speed and direction can then be restricted to a window centered on the background values. The width of the window determines the number of elements in the collection, that is, the computing time, and should be chosen according to the reliability of the background profile and the change rate of the observed system. With the same steps as in the previous paragraph (2 m s^{-1} and 5°), windows with widths of 10 m s^{-1} and 40° require only 54 elements in the collection, which is much more manageable than before.

When no background profile is available (e.g., at the initiation of the process), there are two ways to proceed. One way is to run the algorithm a first time with poor resolution and to use the retrieved profile as the background profile mentioned in the previous paragraph. The advantage is that no external information is required, which renders the algorithm self-consistent. Another way is to divide the whole dataset into independent parts (e.g., sweeps) and to run the method with high reso-

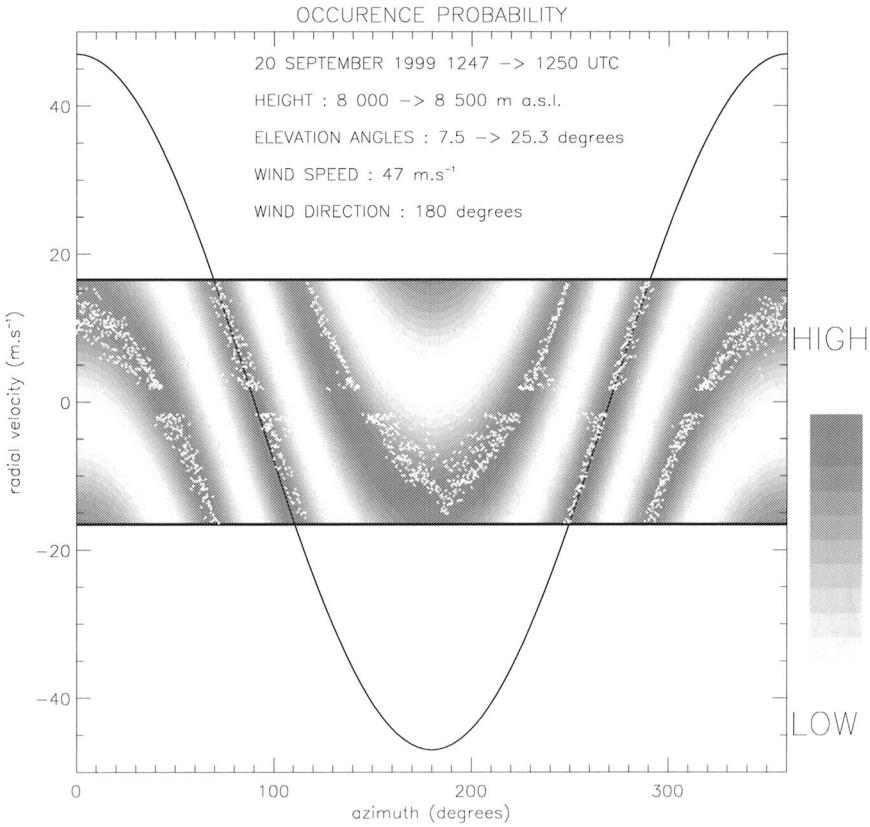

FIG. 2. Illustration of the application of the method on a particular case (1250 UTC 20 Sep 1999) showing the observed radial velocities as functions of the azimuth for heights between 8 and 8.5 km and radar elevation angles between 7.5° and 25.3°. For these elevation angles, the Nyquist velocity is equal to 16.54 m s^{-1}. The retrieved wind speed and direction are, respectively, 47 m s^{-1} and 180°. Superimposed on the graph are the corresponding sine curve and the occurrence probability [$\pi^{ij}(V_r)$] field in the Nyquist interval (black and white isopleths).

lution. At the end of the processing of each part, a check on the probabilities of the elements of the collection is done, and the elements with the lowest probabilities are removed from the collection. Thus, after each part, the number of elements in the collection is decreased, which accelerates the convergence.

This method was tested and validated in Tabary et al. (2000) by comparing the retrieved profiles with the profiles retrieved with the classical VAD analysis. A quality check, based on the number of available measurements and on the standard dispersion of the measurements around the retrieved sine profile, was also implemented in order to discard low-quality retrieved winds.

The present extensive application to the Monte Lema radar data is carried out with a speed increment of 1 m s^{-1} and a direction increment of 3°. The maximum wind speed is set to 50 m s^{-1}, which is sufficient for the systems observed during the MAPSOP. To minimize the influence of the vertical velocity, hydrometeor fall speed, horizontal divergence, and nonlinearities, the analysis is restricted to elevation angles less than 25° and to radar ranges less than 25 km. With this high-resolution numerical setup, it takes, on average, 2 min on a Sun Ultra 60 workstation to retrieve the wind profile from the radar data.

4. Results

The analysis has been run on a 15-min basis on 13 days taken from 10 intensive observation periods:

- IOP2A: 17 and 18 September 1999
- IOP2B: 20 September 1999
- IOP3: 25 and 26 September 1999
- IOP4: 30 September 1999
- IOP5: 3 October 1999
- IOP6: 13 October 1999
- IOP8: 20 and 21 October 1999
- IOP10: 24 October 1999
- IOP15: 6 November 1999
- IOP16: 11 November 1999

This led to an overall dataset of 1248 profiles. Each profile comprises 25 levels, from 0 up to 12 km with a vertical grid spacing of 500 m. The maximum height of the retrieved profile depends on the height of the reflectivity echo tops. Figure 3 presents the contoured

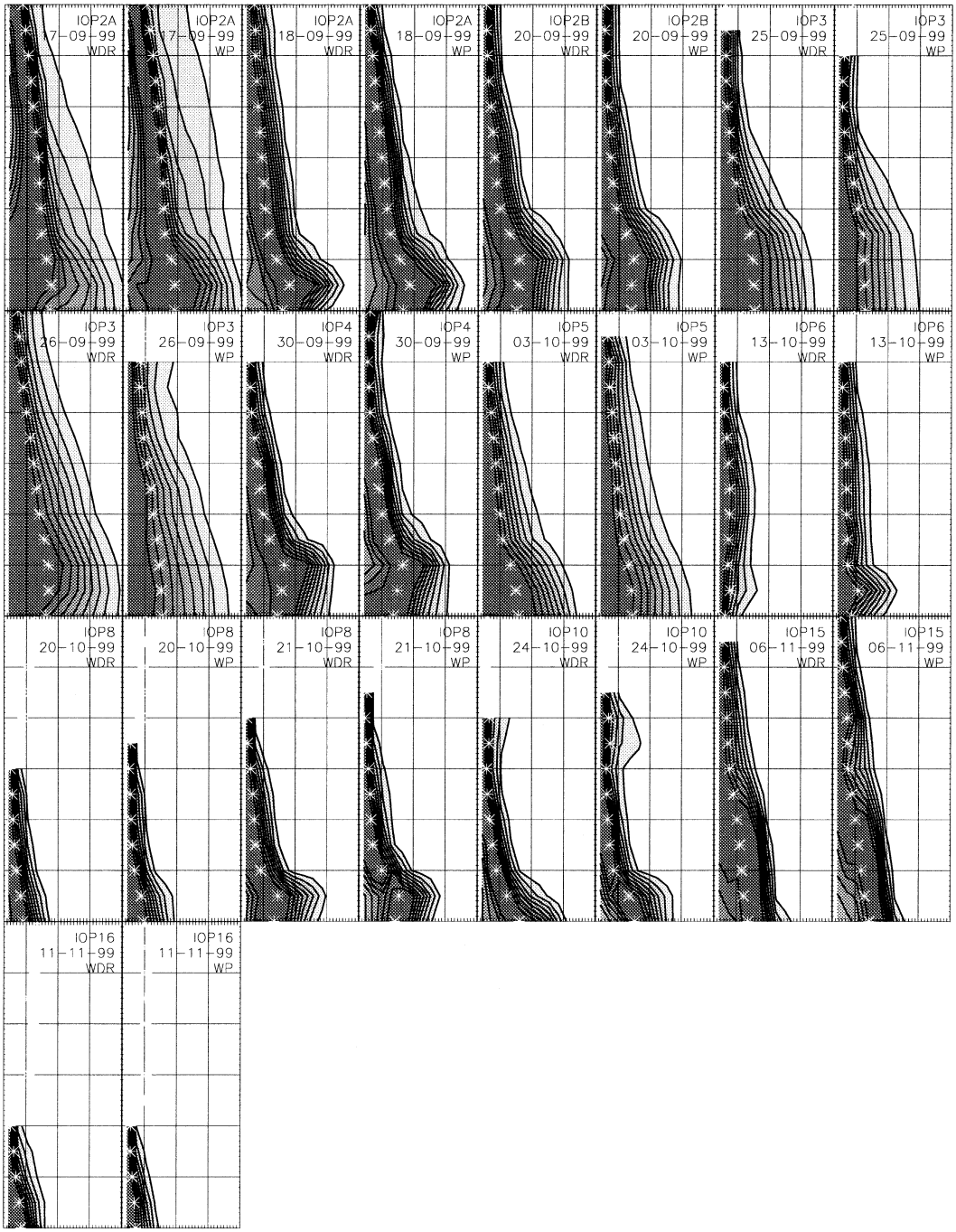

FIG. 3. CFADs (see Yuter and Houze 1995) of radar reflectivity for each of the 13 days considered in the statistical comparison. There are two diagrams per day labeled WDR and WP, each of them being representative of an 80 km $\times$ 80 km domain centered, respectively, on the WDR and on the WP (see Fig. 1). Each diagram starts at the height of 2 km and ends at 8 km. The vertical spacing between two successive horizontal lines is 1 km. The reflectivity axis starts at 15 dBZ and ends at 50 dBZ, and ends the three inner vertical lines indicate the 20-, 30-, and 40-dBZ values. The occurrence frequency was normalized at each height by the maximum frequency of that height. The contours show the 0.1 (outermost); 0.2, 0.3, 0.4, 0.5, 0.6, 0.7, and 0.8 (innermost) normalized occurrence frequency. White stars indicate the averaged profile.

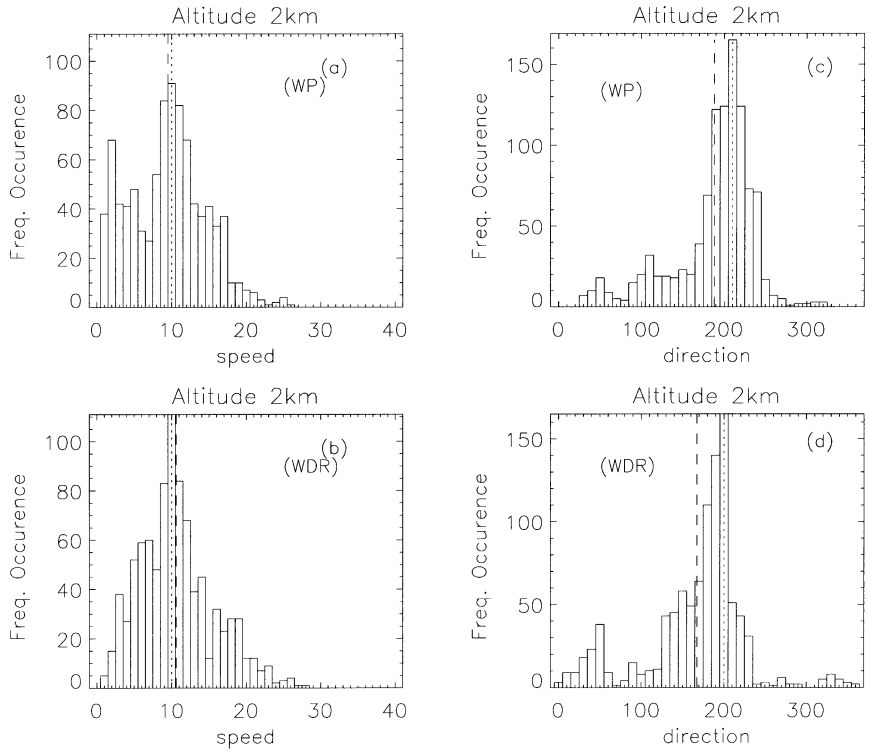

FIG. 4. Histograms of the wind speed and direction for the (a), (c) WP and (b), (d) WDR at 2 km. The dotted line indicates the maximum and the dashed line the mean.

frequency per altitude diagrams (CFADs; Yuter and Houze 1995) of radar reflectivity for each of the 13 days selected for the comparison. For each day two diagrams are shown, each of them being representative of a 80 km $\times$ 80 km region centered on the WDR and the WP, respectively (see Fig. 1). Each diagram starts at the height of 2 km and extends up to 8 km, the vertical spacing between two successive horizontal lines in Fig. 3 being equal to 1 km. The reflectivity axis starts at 15 dBZ and ends at 50 dBZ, and the three inner vertical lines indicate the 20-, 30-, and 40-dBZ values. In order to avoid a strong distortion of the diagrams resulting from an uneven distribution of the number of measurements over height, each profile was normalized at each height by the maximum occurrence frequency at that height. Consequently, the contours shown on Fig. 3 are the 0.1 (outermost), 0.2, 0.3, 0.4, 0.5, 0.6, 0.7, and 0.8 (innermost) normalized occurrence frequency. The averaged vertical profile is represented in each diagram by white stars. For the sake of statistical significance, contours were not drawn when the number of available measurements for that height was below a fixed threshold.

Figure 3 illustrates the large diversity of the observed precipitating systems over the 13 considered days. Some situations were obviously stratiform and showed a well-defined brightband signature and a rather narrow distribution of the reflectivity values at each height (18 and 30 September 1999, 21 October 1999). Some others were evidently convective and were characterized by larger and more broadly distributed reflectivity values, especially at low levels (17 and 25 September 1999, 3 October 1999). When interpreting those diagrams, it should nonetheless be kept in mind that they represent averages over a 24-h period and over an 80 km $\times$ 80 km domain and may include both convective and stratiform components. The height of the sampled precipitation systems also greatly varies over the considered period. The important variety of the sampled precipitating system is an advantage in the present context, since it allows testing of the Bayesian method under very different conditions and makes its evaluation more objective.

Finally, despite the fact that the two domains used (centered, respectively, on the WDR and on the WP) are rather large (80 km $\times$ 80 km) and overlap. Fig. 3 shows some significant differences between the WDR and WP diagrams. In most cases, the diagram for the WDR extends higher and shows larger reflectivity values, which is in good agreement with the typical rain distribution for that region during fall (Frei and Schär 1998). These different precipitation conditions might be responsible for some of the observed differences between the WDR and the WP wind profiles.

The histograms of the wind speed and direction at 2 and 5 km are shown in Figs. 4 and 5, respectively. The top (bottom) parts of Figs. 4 and 5 correspond to the WP (WDR) measurements. There is relatively good

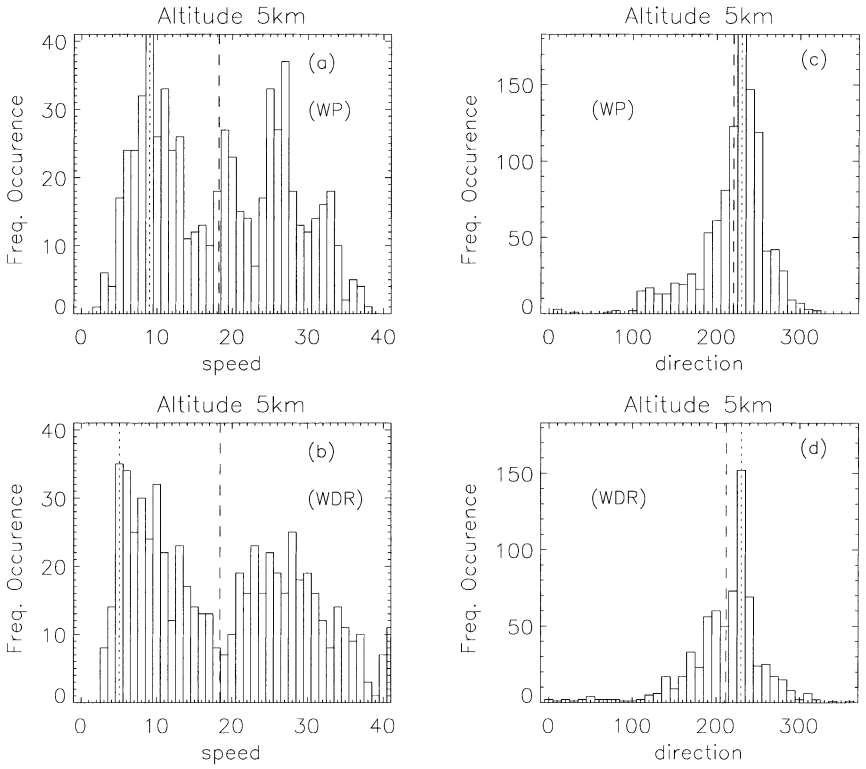

FIG. 5. Same as in Fig. 4 but at 5 km.

agreement between the different histograms of the WDR and WP in terms of general shape, location of the maximum (indicated by a dotted line), value of the mean (indicated by a dashed line), and location of secondary maxima. The histograms of the wind direction for all graphs (Figs. 4c,d, 5c,d) exhibit a strong maximum between 200° and 230°, which is not surprising, because the IOPs selected for the comparison all correspond to precipitation events in the southern Alps. Given the mesoscale topography, these precipitation events are more likely to occur under a southerly flow regime that pushes the warm and moist Mediterranean air masses up the alpine slopes (Frei and Schär 1998). At 5 km (Figs. 5c,d), the maximum on both histograms is reached exactly for the same wind direction (230°). On the other hand, at 2 km, a close examination of the wind direction histograms (Figs. 4c,d) reveals some significant differences. The WDR data show a larger dispersion than the WP data, and the mean (dashed line) and the maximum (dotted line) of the wind direction histogram at 2 km appear to be shifted by about 15°–20° between the WP and the WDR. Finally, while the histograms for the wind direction appear to be basically unimodal, the histograms for the wind speed at 5 km (Figs. 5a,b) exhibit two maxima, one at about 10 m s^{-1} and an other at about 28 m s^{-1}. A third maximum can be distinguished at about 20 m s^{-1} on the WP histogram that corresponds to a well-defined minimum on the WDR histogram.

Figure 6 shows the scatterplots of the wind speed (Fig. 6a), wind direction (Fig. 6b), zonal wind (Fig. 6c), and meridional wind (Fig. 6d) as deduced from the WDR data and measured with the WP. All quality-checked data corresponding to all altitudes and all IOPs have been taken into account, except in the wind direction scatterplot, where low wind speed measurements (less than 3 m s^{-1}) have been removed because of the poor correlation of the large observed difference. The discretization of the wind speeds (every 1 m s^{-1}) and directions (every 3°) required by the Bayesian VAD is obvious in Figs. 6a and 6b. There is a qualitative good agreement between the two instruments. The correlation coefficients r for the wind speed, meridional wind, and zonal wind (the values of which are indicated on each diagram of Fig. 6) are, respectively, equal to 0.92, 0.93, and 0.91. The correlation coefficient drops to 0.79 for the wind direction, but this is evidently due to the 360° discontinuity of the value of the wind direction around the north. Some outliers can be seen on the wind direction scatterplot (Fig. 6b) for WDR wind directions (vertical axis) below 30°, above 320°, and around 100°. Whereas the first two groups of outliers mainly correspond to 2-km measurements, which is consistent with the differences noted between the histograms at 2 km (Figs. 4c,d), the third one is associated with 3-km measurements. Further work is needed (e.g., stratification with IOPs) to determine the origin of the scatter at that height.

In order to make the comparison more quantitative,

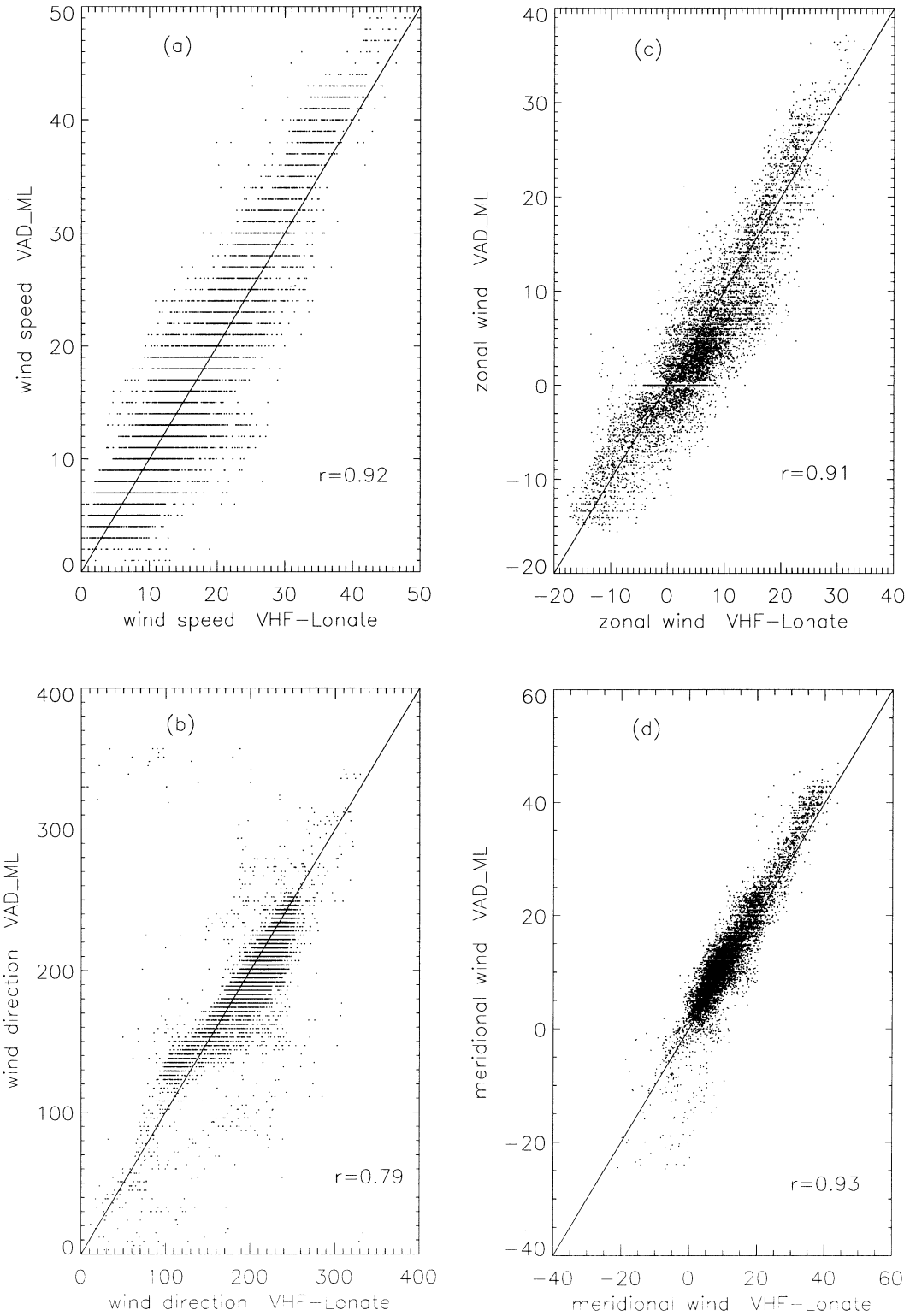

FIG. 6. Scatterplots of the (a) wind speed (m s^{-1}), (b) wind direction (°) (clockwise from the north), (c) zonal wind (m s^{-1}), and (d) meridional wind (m s^{-1}), as derived from the WDR and measured with the WP. Low-intensity measurements have been removed from the wind direction scatterplot because of the poor significance of the large observed differences. The value of the correlation coefficient *r* is indicated on each scatterplot.

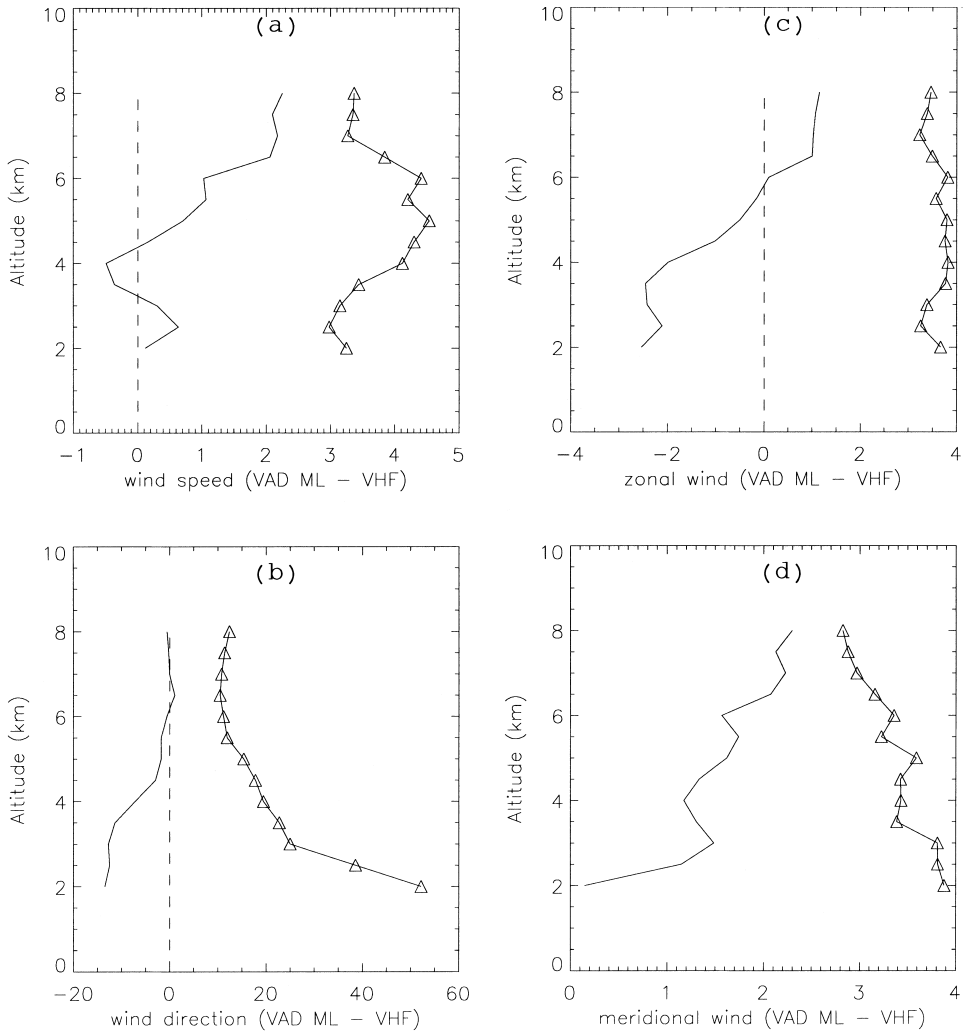

FIG. 7. Mean (solid curve) and std dev (triangles) of the differences between the WDR and the WP (WDR minus WP) in terms of (a) wind speed (m s^{-1}), (b) wind direction (°), (c) zonal wind (m s^{-1}), and (d) meridional wind (m s^{-1}).

Fig. 7 displays the mean and standard deviation of the observed differences between the WDR and the WP (WDR minus WP) in terms of wind speed (Fig. 7a), wind direction (Fig. 7b), zonal wind (Fig. 7c), and meridional wind (Fig. 7d) as functions of height. Because of the altitude of the Monte Lema radar (1625 m) and because of the blind range of the WP (up to 1800 m), each profile starts at the height of 2 km. The number of common measurements steadily decreases with height from more than 1000 at 2 km down to a few tens at 8 km. Profiles are not shown above 8 km because it was estimated that the number of common measurements was too small to make the statistical comparison significant. More generally, this regular decrease in the number of common measurements makes the observed differences less significant in altitude than at lower levels. The standard deviations of the wind speed, zonal wind, and meridional wind differences (Figs. 7a,c,d) are very consistent with each other. They are nearly constant with height and vary between 3 and 4 m s^{-1}. On the contrary, the standard deviation of the wind direction (Fig. 7b) shows a clear dependence on the altitude, decreasing from about 50° at 2 km down to 10° at 8 km. These large values of the standard deviation observed at low levels (up to 4 km) can be explained by the fact that the WP is located over the plains, whereas the WDR is in the alpine upslope region where the flow is likely to be deflected or lifted by the orography.

The bias in the wind direction at low levels, already noted in the histograms in Fig. 4, is clearly evidenced in Fig. 7b. It is approximately equal to 15° up to 5 km, where it drops to 0°. In the case of a general southerly flow (which is the dominant mode; see Fig. 5), a veering of the wind occurs as the flow moves northward toward the Alps (see Fig. 1). This cyclonic rotation of the flow was also evidenced in the multiple-Doppler analyses of

Chong et al. (2000) during some IOPs of the special observing period (see, e.g., Figs. 5 and 8 of Chong et al. 2000). Most of these cases were characterized by a low-level (up to 2 km) southeasterly flow, coming from the Adriatic Sea, capped by a southwesterly flow coming from the Ligurian Sea. The observed bias in the low-level wind direction between the WDR and the WP might therefore be explained by the upslope lifting of this low-level Adriatic flow at the location of the WDR. Under that assumption, for heights between 2 and 4 km, the WP measures only the Ligurian component (i.e., from the southwest), while the flow at the same height above the WDR contains a contribution of the Adriatic component (i.e., veering the wind to the southeast).

The wind speed difference (Fig. 7a) does not exhibit any clear dependence with height, except above 5 km where it is steadily increasing up to 2 m s^{-1}, which means that, at these heights, the WDR wind speed estimation is always higher than the WP wind speed measurement. It should, however, be noted that this bias is observed above 5–6 km, where the scarcity of WDR measurements makes its physical significance questionable.

5. Summary

The present paper is part of a series devoted to the exploration of the possible ways to combine WDR and WP data and to take advantage of their complementarity. The MAP dataset is used to evaluate the potential of the different approaches.

In this paper, we have carried out a statistical comparison between the wind profiles measured by the French VHF INSU/Météo-France WP and deduced from the Swiss C-band Monte Lema WDR using a new Bayesian VAD-based technique. More than 1200 simultaneous profiles taken from 13 days of the MAP field phase have been considered in the analysis. The objectives were 1) to extensively test and validate this new potentially operational technique and 2) to infer some statistical properties of the wind profile during precipitation events in the southern Alps. The main conclusions can be summarized as follows.

- This extensive application of the Bayesian VAD confirms its great operational potential. Even under extreme conditions (e.g., during IOP2B, the wind speed reached 50 m s^{-1}, which means that the Monte Lema radial velocities are folded twice), the wind speed and direction are well recovered. The correlation coefficients between the WDR and the WP wind profiles are higher than 0.9. The main advantage of the Bayesian VAD over existing linear analysis (VAD, VVP, . . .) is that *it does not require any preliminary dealising of the radial velocities.* Since dealiasing radial velocity is a time-consuming process, this original feature makes it very well suited to real-time operational purposes. There are, of course, a number of drawbacks: the constant term of the VAD expansion has to be explicitly specified, only the wind profile can be retrieved, and the analysis has to be performed at the radar location. This technique could be used in the following ways:
  1) application of the Bayesian VAD to the raw radar data and retrieval of the wind profile;
  2) use of the retrieved wind profile as the reference basis dealiasing algorithms need to correctly edit the data; and
  3) application of the classical VAD, VVP, or any other technique to recover the full set of kinematic parameters (divergence, deformation, . . .) from the dealiased radar dataset.
- At 5 km, that is, above the highest alpine peak, the histograms of the wind direction for the selected cases, which all correspond to precipitation events in the Lago Maggiore Target Area, exhibit a clear unimodal distribution centered on about 220° for both instruments, which is in good agreement with the proposed scenario for heavy precipitation in the southern Alps (Frei and Schär 1998). On the other hand, the histograms of the wind speed at the same height (5 km) appear to be bimodal, with one peak at about 10 m s^{-1} and an other at 28 m s^{-1}.
- The examination of the mean and standard deviation of the observed differences in terms of wind speed and direction shows a good agreement between the two instruments. The standard deviations of the wind components are about 3–4 m s^{-1}, but they are also strongly dependent on the weaker regime (e.g., convective/stratiform). A bias of about 15° up to 4–5 km was observed in the wind direction between the two instruments. In the case of a general southerly flow, which is the most frequent flow regime during precipitation events, the flow experiences a cyclonic deflection as it impinges upon the alpine barrier. This statistical finding is in good agreement with some of the multiple-Doppler analyses performed during the MAP field phase (Chong et al. 2000). Further work is needed to fully understand the nature of that orographic forcing on the mesoscale flow.

Acknowledgments. We are indebted to Esther Häller (MAP Data Center), who kindly provided the whole set of Monte Lema radar data in proper form, to Vladislav Klaus (Météo-France/CNRM) for fruitful discussions about the wind profiler data, and to David Weissenbach (CETP) for his assistance during the numerical implementation and testing of the Bayesian VAD. We have also greatly benefited from the comments and remarks of three anonymous reviewers.

REFERENCES

Battan, L. J., 1977: Rain resulting from melting ice particles. *J. Appl. Meteor.,* **16,** 595–604.

Bougeault, P., and Coauthors, 2001: The MAP Special Observing Period. *Bull. Amer. Meteor. Soc.*, **82,** 433–462.

Browning, K. A., and R. Wexler, 1968: The determination of kinematic properties of a wind field using Doppler radar. *J. Appl. Meteor.*, **7,** 105–113.

Caccia, J.-L., and Coauthors, 2001: The French ST-Radar Network during MAP: Observational and scientific aspects. *Meteor. Z.*, **10,** 469–478

Chong, M., and Coauthors, 2000: Real-time wind synthesis from Doppler radar observations during the Mesoscale Alpine Programme. *Bull. Amer. Meteor. Soc.*, **81,** 2953–2962.

Doviak, R. J., and D. S. Zrnić, 1984: *Doppler Radar and Weather Observations.* Academic Press, 458 pp.

Frei, C., and C. Schär, 1998: A precipitation climatology of the Alps from high resolution rain-gauge observations. *Int. J. Climatol.*, **18,** 873–900.

Guillemette, P., and I. Zawadzki, 1999: Integration of UHF profiler information with bistatic measurements. Preprints, *29th Conf. on Radar Meteorology*, Montreal, QC, Canada, Amer. Meteor. Soc., 142–144.

Joss, J., and Coauthors, 1998: Operational use of radar for precipitation measurements in Switzerland. Final Rep. NRP31, ETH Zürich, 108 pp.

Lhermitte, R. M., and D. Atlas, 1961: Precipitation motion by pulse Doppler. *Proc. Ninth Conf. on Radar Meteorology*, Kansas City, MO, Amer. Meteor. Soc., 218–223.

Mood, A. M., F. A. Graybill, and D. C. Boes, 1963: *Introduction to the Theory of Statistics.* Mc Graw-Hill, 339–350.

Petitdidier, M., P. Tabary, J. Bigorgne, G. Scialom, and V. Klaus, 2000: Integration of the VHF wind profiler data within dual-Doppler wind synthesis. *Phys. Chem. Earth*, **25,** 1195–1199.

Rossa, A., 2000: COST-717: Use of radar observations in hydrological and NWP models. *Phys. Chem. Earth*, **25,** 1221–1224.

Serafin, R. J., and J. W. Wilson, 2000: Operational weather radar in the United States: Progress and opportunity. *Bull. Amer. Meteor. Soc.*, **81,** 501–518.

Tabary, P., G. Scialom, and K. Van der Straeten, 2000: A comparative study of two new approaches to estimate the wind profile from aliased radial velocities. *Phys. Chem. Earth*, **25,** 1215–1220.

Waldteufel, P., and H. Corbin, 1979: On the analysis of single-Doppler radar data. *J. Appl. Meteor.*, **18,** 532–542.

Yuter, S. E., and R. A. Houze Jr., 1995: Three-dimensional kinematic and microphysical evolution of Florida cumulonimbus. Part II: Frequency distributions of vertical velocity, reflectivity and differential reflectivity. *Mon. Wea. Rev.*, **123,** 1941–1963.